Supplementary Text: The H content of aubrites

Liam D. Peterson[a,*], Megan E. Newcombe[a], Conel M. O'D. Alexander[b], Jianhua Wang[b], Frieder Klein[d], David V. Bekaert[c,e,f], Sune G. Nielsen[c,e]

[a] Department of Geology, University of Maryland, College Park, MD 20740, United States

[b] Earth and Planets Laboratory, Carnegie Institution for Science, Washington, DC 20015, United States

[c] NIRVANA Labs, Woods Hole Oceanographic Institution, Woods Hole, MA 02540, United States

[d] Department of Marine Chemistry and Geochemistry, Woods Hole Oceanographic Institution, Woods Hole, MA 02540, United States

[e]Department of Geology and Geophysics, Woods Hole Oceanographic Institution, Woods Hole, MA 02540, United States

[f] Université de Lorraine, CNRS, CRPG, 54000 Nancy, France

S1) Miller Range 13004 albitic glass

Within one of our aliquots of Miller Range (MIL) 13004, we analyzed albitic glass which was commonly associated with fractures and voids and is present as a minor to trace phase. Prior work has identified albitic glasses in aubrites, including MIL 13004 (Wilbur et al., 2022), which is commonly interpreted as a product of partial melting on the aubrite parent body. We find higher SiO_2 (74 wt.% vs. 67.8 wt.%) and Al_2O_3 (21 wt.% vs. 17.9 wt.%) contents and much

lower Na_2O (3.9 wt.% vs. 10.97 wt.%) contents in albitic glass from our aliquot of MIL 13004 albitic glass (Table 4) than the values reported by Wilbur et al. (2022). We suggest this discrepancy in major element compositions likely reflects heterogeneity in glass compositions between sample aliquots as our measured values resemble the L871 glass of Fogel (2005), but a systematic study on several aliquots is needed to validate this hypothesis. Overall, albitic melts in aubrites have been suggested to be the product of high degrees of partial melting (≤ 50%) and late-stage melts (Fogel, 2005; Keil et al., 2011). The H_2O contents (~0.6 – 3.3 µg/g) of the MIL 13004 albitic glass are below the LOD (see Section 4.2) and have highly variable F (~95 – 190 µg/g) and Cl contents (560 – 640 µg/g) that are consistent across the 01/22 and 02/22 analytical sessions (Table S3, analyses 483 – 491; Table S5, analysis 1034). The F contents of the albitic glass are about 1 to 2 orders of magnitude higher than all other analyzed phases and the Cl contents are several orders of magnitude higher (Table 5). The origin of these high halogen contents is unclear, but it may be the result of interaction with a halogen rich-fluid on the aubrite parent body, partial dissolution of halogen rich sulfides such as djerfisherite, or terrestrial weathering and alteration (e.g., Krähenbühl et al., 1998; Velbel, 2014). If we are to consider equilibrium with respect to H_2O between the albitic glass (~0.6 – 3.3 µg/g H_2O) and enstatite (5±2 µg/g H_2O; 1 SD) in MIL 13004, then we have a minimum apparent mineral-melt H_2O partition coefficient $\left(D = \frac{[H_2O]_{mineral}}{[H_2O]_{melt}}\right)$ of ~0.9, which is orders of magnitude higher than experimentally determined mineral-melt partition coefficients for enstatite (Grant et al., 2006) and orthopyroxene (e.g., Aubaud et al., 2004; Grant et al., 2007; Hauri et al., 2006). This either reflects disequilibrium between the minerals and the melt for H_2O or previously uncharacterized partitioning behavior for H_2O at low total H_2O contents or pressure, as has been suggested for natural and experimental samples (Peterson et al., 2023; Sarafian et al., 2019). More

experimental work is required to evaluate these possibilities. Nevertheless, we elect to exclude these values for the albitic glass as they may represent disequilibrium, could have low H_2O contents as the result of production as a high-degree or late-stage partial melt, and the estimates for glass H_2O contents based upon experimentally derived partition coefficients give a higher estimate (~1500 µg/g H_2O vs. < ~3.3 µg/g H_2O). Notably, if we were to use the measured value of MIL 13004 albitic glass in our estimates for the bulk H_2O contents of aubrites, our bulk estimates would be lowered in glass-bearing cases (see Sections 5.1.3 and 5.2), thereby not affecting our conclusions.

S2) Potential, non-NAM, carriers of H in aubrites

We analyzed H_2O in enstatite, forsterite, diopside, and plagioclase in aubrites. NAMs constitute >~99 vol. % of aubrites on average; however, it is possible that other minor or trace phases (e.g., glass, sulfides, or metal) could concentrate water and represent major contributions to aubrite water budgets despite their low abundances. We consider this possibility in the following section.

S2.1 Other silicate minerals

On average, aubrites are ~75 – 98 vol. % enstatite (Keil, 2010) and lack primary hydrous phases. Rare instances of secondary fluor-amphibole (Bevan et al., 1977; Graham et al., 1977) and roedderite (Fogel, 2002; Hsu, 1998), which may reflect igneous crystallization or a low temperature event, have been identified in aubrites. Notably, fluor-amphibole has only been identified in vugs in Mayo Belwa, an impact melt breccia, and is nearly end-member fluororichterite (Bevan et al., 1977; Graham et al., 1977; Rubin, 2010). Considering that vugs in Mayo Belwa are modestly abundant (< 5 vol. %), not all vugs contain fluor-amphibole, vugs

commonly contain several phases (Rubin, 2010), the fluor-amphibole is nearly end-member fluororichterite, indicating the W position in the structure is composed almost entirely of F instead of OH, and fluor-amphibole has only been identified as a secondary phase in Mayo Belwa, it likely constitutes a negligible contribution to the bulk H_2O content of average aubritic materials. Due to the rarity and potentially secondary origin of amphibole in Mayo Belwa, we suggest it is likely not reflective of the H_2O content of average aubritic material. Despite being an end-member in the H_2O-bearing Milarite-type mineral group (Gagné and Hawthorne, 2016; Seifert and Schreyer, 1969), we do not consider roedderite (end-member empirical formula: $Na_{1.5}K_{0.5}Mg_{3.75}Fe^{2+}_{1.25}Si_{12}O_{30}$) as a major carrier of H_2O as: 1) there is no clear indication of H_2O in the roedderite structure (Forbes et al., 1972); and 2) the H_2O contents of Milarite-type minerals are poorly constrained and many species are anhydrous (Gagné and Hawthorne, 2016). Therefore, any primary H_2O (or other H-bearing species) in aubrites is likely to be hosted in NAMs, silicate glass, sulfides, and FeNi metal. For phases not analyzed in this study, we provide a first order estimate of their H_2O contents based upon our measured H_2O concentrations and experimentally determined partition coefficients.

S2.2 Silicate glass

We can provide a first order estimate of the H_2O content of unmeasured phases by assuming all unmeasured phases are in equilibrium with enstatite and that partition coefficients determined under terrestrial conditions are applicable to aubrite parent bodies (see Section S3). We select enstatite as our reference mineral instead of forsterite or feldspar as our phase average for enstatite is based upon 86 analyses across all seven aubrites investigated compared to 4 analyses for feldspar, and 3 analyses for forsterite. Using our measured enstatite H_2O contents and published partition coefficients (Dobson et al., 1995), we estimate that silicate glass in

equilibrium with enstatite would contain ~1500 µg/g H_2O. If we instead use Shallowater plagioclase (24 µg/g H_2O) as our reference phase, then we estimate that silicate glass would contain ~628 µg/g H_2O (Lin et al., 2019). We note, that with the exception of a feldspathic clast in LAR 04316, silicate glass is absent or a trace phase in aubrites (Keil, 2010), thereby limiting the contribution of silicate glass to the H_2O budget of aubrites.

S2.3 Metals and sulfides

Previous studies have experimentally constrained the partitioning of H between metal and silicate and suggest that H is incompatible in Fe metal at low pressures (Clesi et al., 2018; Gaillard et al., 2022; Li et al., 2015; Malavergne et al., 2019; Okuchi, 1997; Tagawa et al., 2021). We are unaware of any studies that experimentally constrain sulfide – silicate H partitioning. Therefore, we assume that metal and sulfides have similar H_2O partition coefficients. By combining our measured enstatite, forsterite, diopside, and feldspar H_2O contents, calculated glass H_2O contents (Table 6), and the modal mineralogy of our samples (Table 2), we estimate that the silicate portions of our analyzed main group aubrites all contain < ~5 µg/g H_2O (Supplementary File "Aubs_calcs.xlsx"). We take a metal – silicate H partition coefficient of 0.22 (Gaillard et al., 2022) and our calculated silicate H_2O contents (~5 µg/g H_2O), which yield metal and sulfide H_2O (quantified from total H) concentrations of ~1 µg/g. Metal and sulfides in aubrites are minor to trace phases (Keil, 2010), and the low estimated H_2O content (~1 µg/g H_2O) suggests metal and sulfide in aubrites are unlikely to be an abundant source of H_2O in aubrites. Overall, we suggest trace silicate material (Section S2.1), silicate glass (Section S2.2), and metals and sulfides are either too low in abundance or too H_2O poor to serve as major reservoirs of H_2O in aubrites.

S3) Do our H_2O analyses reflect equilibrium or disequilibrium in aubrite NAMs?

Despite experimentally determined partition coefficients permitting equilibrium between the phases measured in this study (Section 5.1.3), it is possible that the measured H_2O concentrations in NAMs have been disturbed by disequilibrium processes such as H-loss due to thermal metamorphism or shock heating or H-enrichment due to hydrothermal alteration. To a first order, if disequilibrium processes affected our grains, we would expect to observe gradients in H_2O concentrations across grains, however, for samples where transects could be measured (i.e., MIL 13004, Norton County, Shallowater), no H_2O gradients are observed (Fig. S12 – S16). Aubrite enstatite H_2O contents exhibit a weak correlation with degree of shock (Fig. 2B), which may suggest that aubrite H_2O contents could have been modified by secondary processes. Notably, any thermal process (e.g., shock heating, thermal metamorphism) would be expected to reduce the H_2O content of aubrite silicates, resulting in normal zonation, which is not observed. Therefore, we suggest that H-loss processes such as thermal metamorphism or shock heating are unlikely to have caused major modifications to the measured H_2O contents of our NAMs. It is also possible that aubrite silicates may have undergone H-enrichment during hydrothermal events. However, hydrous phases are rare in aubrites and are of an unclear origin (see Section 5.3.1; Keil, 2010), arguing against any widespread hydrothermal events on aubrite parent bodies. Overall, we suggest that the effect of secondary processes on the measured H_2O concentrations is likely minimal. Furthermore, regardless of whether or not our analyses reflect equilibrium, our analyses represent the most accurate determination of aubrite silicate H_2O contents, allowing for more precise evaluations of bulk Aubrite H_2O contents and the potential for H-delivery to the Earth by aubrite-like material.

References

Aubaud, C., Hauri, E.H., Hirschmann, M.M., 2004. Hydrogen partition coefficients between nominally anhydrous minerals and basaltic melts. Geophysical Research Letters 31, 1–4. https://doi.org/10.1029/2004GL021341

Bevan, A.W.R., Bevan, J.C., Francis, J.G., 1977. Amphibole in the Mayo Belwa meteorite: first occurrence in an enstatite achondrite. Mineralogical Magazine 41, 531–534. https://doi.org/10.1180/minmag.1977.041.320.20

Clesi, V., Bouhifd, M.A., Bolfan-Casanova, N., Manthilake, G., Schiavi, F., Raepsaet, C., Bureau, H., Khodja, H., Andrault, D., 2018. Low hydrogen contents in the cores of terrestrial planets. Science Advances 4, e1701876. https://doi.org/10.1126/sciadv.1701876

Dobson, P.F., Skogby, H., Rossman, G.R., 1995. Water in boninite glass and coexisting orthopyroxene: concentration and partitioning. Contr. Mineral. and Petrol. 118, 414–419. https://doi.org/10.1007/s004100050023

Fogel, R.A., 2005. Aubrite basalt vitrophyres: The missing basaltic component and high-sulfur silicate melts. Geochimica et Cosmochimica Acta 69, 1633–1648. https://doi.org/10.1016/j.gca.2003.11.032

Fogel, R.A., 2002. The Composition of Roedderite in Aubrites. Meteoritics and Planetary Science Supplement 37, A48.

Forbes, W.C., Baur, W.H., Khan, A.A., 1972. Crystal chemistry of milarite-type minerals. American Mineralogist 57, 463–472.

Gagné, O.C., Hawthorne, F.C., 2016. Chemographic Exploration of the Milarite-type Structure. The Canadian Mineralogist 54, 1229–1247. https://doi.org/10.3749/canmin.1500088

Gaillard, F., Malavergne, V., Bouhifd, M.A., Rogerie, G., 2022. A speciation model linking the fate of carbon and hydrogen during core – magma ocean equilibration. Earth and Planetary Science Letters 577, 117266. https://doi.org/10.1016/j.epsl.2021.117266

Graham, A.L., Easton, A.J., Hutchison, R., 1977. The Mayo Belwa meteorite: a new enstatite achondrite fall. Mineralogical Magazine 41, 487–492. https://doi.org/10.1180/minmag.1977.041.320.10

Grant, K.J., Kohn, S.C., Brooker, R.A., 2007. The partitioning of water between olivine, orthopyroxene and melt synthesised in the system albite–forsterite–H2O. Earth and Planetary Science Letters 260, 227–241. https://doi.org/10.1016/j.epsl.2007.05.032

Grant, K.J., Kohn, S.C., Brooker, R.A., 2006. Solubility and partitioning of water in synthetic forsterite and enstatite in the system MgO–SiO2–H2O±Al2O3. Contrib Mineral Petrol 151, 651–664. https://doi.org/10.1007/s00410-006-0082-7

Hauri, E.H., Gaetani, G.A., Green, T.H., 2006. Partitioning of water during melting of the Earth's upper mantle at H2O-undersaturated conditions. Earth and Planetary Science Letters 248, 715–734. https://doi.org/10.1016/j.epsl.2006.06.014

Hsu, W., 1998. Geochemical and petrographic studies of oldhamite, diopside, and roedderite in enstatite meteorites. Meteoritics & Planetary Science 33, 291–301. https://doi.org/10.1111/j.1945-5100.1998.tb01633.x

Keil, K., 2010. Enstatite achondrite meteorites (aubrites) and the histories of their asteroidal parent bodies. Geochemistry 70, 295–317. https://doi.org/10.1016/j.chemer.2010.02.002

Keil, K., McCOY, T.J., Wilson, L., Barrat, J.-A., Rumble, D., Meier, M.M.M., Wieler, R., Huss, G.R., 2011. A composite Fe,Ni-FeS and enstatite-forsterite-diopside-glass vitrophyre

clast in the Larkman Nunatak 04316 aubrite: Origin by pyroclastic volcanism. Meteoritics & Planetary Science 46, 1719–1741. https://doi.org/10.1111/j.1945-5100.2011.01261.x

Krähenbühl, U., Noll, K., Döbeli, M., Grambole, D., Herrmann, F., Tobler, L., 1998. Exposure of Allan Hills 84001 and other achondrites on the Antarctic ice. Meteoritics & Planetary Science 33, 665–670. https://doi.org/10.1111/j.1945-5100.1998.tb01671.x

Li, Y., Dasgupta, R., Tsuno, K., 2015. The effects of sulfur, silicon, water, and oxygen fugacity on carbon solubility and partitioning in Fe-rich alloy and silicate melt systems at 3 GPa and 1600 °C: Implications for core–mantle differentiation and degassing of magma oceans and reduced planetary mantles. Earth and Planetary Science Letters 415, 54–66. https://doi.org/10.1016/j.epsl.2015.01.017

Lin, Y.H., Hui, H., Li, Y., Xu, Y., van Westrenen, W., 2019. A lunar hygrometer based on plagioclase-melt partitioning of water. Geochem. Persp. Let. 10, 14–19. https://doi.org/10.7185/geochemlet.1908

Malavergne, V., Bureau, H., Raepsaet, C., Gaillard, F., Poncet, M., Surblé, S., Sifré, D., Shcheka, S., Fourdrin, C., Deldicque, D., Khodja, H., 2019. Experimental constraints on the fate of H and C during planetary core-mantle differentiation. Implications for the Earth. Icarus 321, 473–485. https://doi.org/10.1016/j.icarus.2018.11.027

Okuchi, T., 1997. Hydrogen Partitioning into Molten Iron at High Pressure: Implications for Earth's Core. Science 278, 1781–1784. https://doi.org/10.1126/science.278.5344.1781

Peterson, L.D., Newcombe, M.E., Alexander, C.M.O., Wang, J., Sarafian, A.R., Bischoff, A., Nielsen, S.G., 2023. The H2O content of the ureilite parent body. Geochimica et Cosmochimica Acta 340, 141–157. https://doi.org/10.1016/j.gca.2022.10.036

Rubin, A.E., 2010. Impact melting in the Cumberland Falls and Mayo Belwa aubrites. Meteoritics & Planetary Science 45, 265–275. https://doi.org/10.1111/j.1945-5100.2010.01022.x

Sarafian, A.R., Nielsen, S.G., Marschall, H.R., Gaetani, G.A., Righter, K., Berger, E.L., 2019. The water and fluorine content of 4 Vesta. Geochimica et Cosmochimica Acta, A GCA special volume in honor of Professor Lawrence A. Taylor 266, 568–581. https://doi.org/10.1016/j.gca.2019.08.023

Seifert, F., Schreyer, W., 1969. Stability relations of K2Mg5Si12O30, and end member of the merrihueite-roedderite group of meteoritic minerals. Contr. Mineral. and Petrol. 22, 190–207. https://doi.org/10.1007/BF00387953

Tagawa, S., Sakamoto, N., Hirose, K., Yokoo, S., Hernlund, J., Ohishi, Y., Yurimoto, H., 2021. Experimental evidence for hydrogen incorporation into Earth's core. Nat Commun 12, 2588. https://doi.org/10.1038/s41467-021-22035-0

Velbel, M.A., 2014. Terrestrial weathering of ordinary chondrites in nature and continuing during laboratory storage and processing: Review and implications for Hayabusa sample integrity. Meteoritics & Planetary Science 49, 154–171. https://doi.org/10.1111/j.1945-5100.2012.01405.x

Wiens, T., 2021. Linear Regression with Errors in X and Y.

Wilbur, Z.E., Udry, A., McCubbin, F.M., vander Kaaden, K.E., DeFelice, C., Ziegler, K., Ross, D.K., McCoy, T.J., Gross, J., Barnes, J.J., Dygert, N., Zeigler, R.A., Turrin, B.D., McCoy, C., 2022. The effects of highly reduced magmatism revealed through aubrites. Meteoritics & Planetary Science 57, 1–34. https://doi.org/10.1111/maps.13823

York, D., Evensen, N.M., Martínez, M.L., De Basabe Delgado, J., 2004. Unified equations for the slope, intercept, and standard errors of the best straight line. American Journal of Physics 72, 367–375. https://doi.org/10.1119/1.1632486

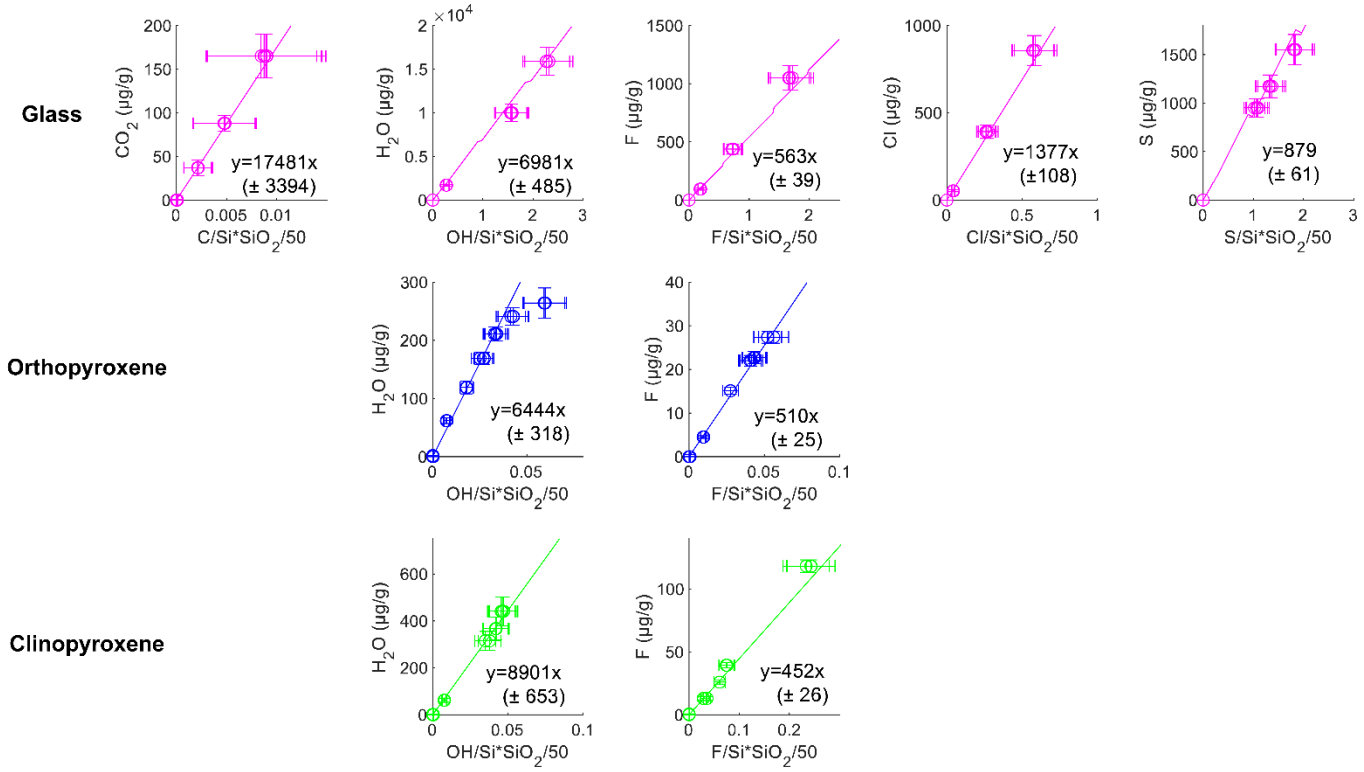

232

233 ***Fig. S1)*** Calibration curves for CO_2, H_2O, F, Cl, and S for glass, orthopyroxene, and

234 clinopyroxene in the 01/22 analytical session. Uncertainties on slopes were determined using a

235 York regression (Wiens, 2021; York et al., 2004).

236

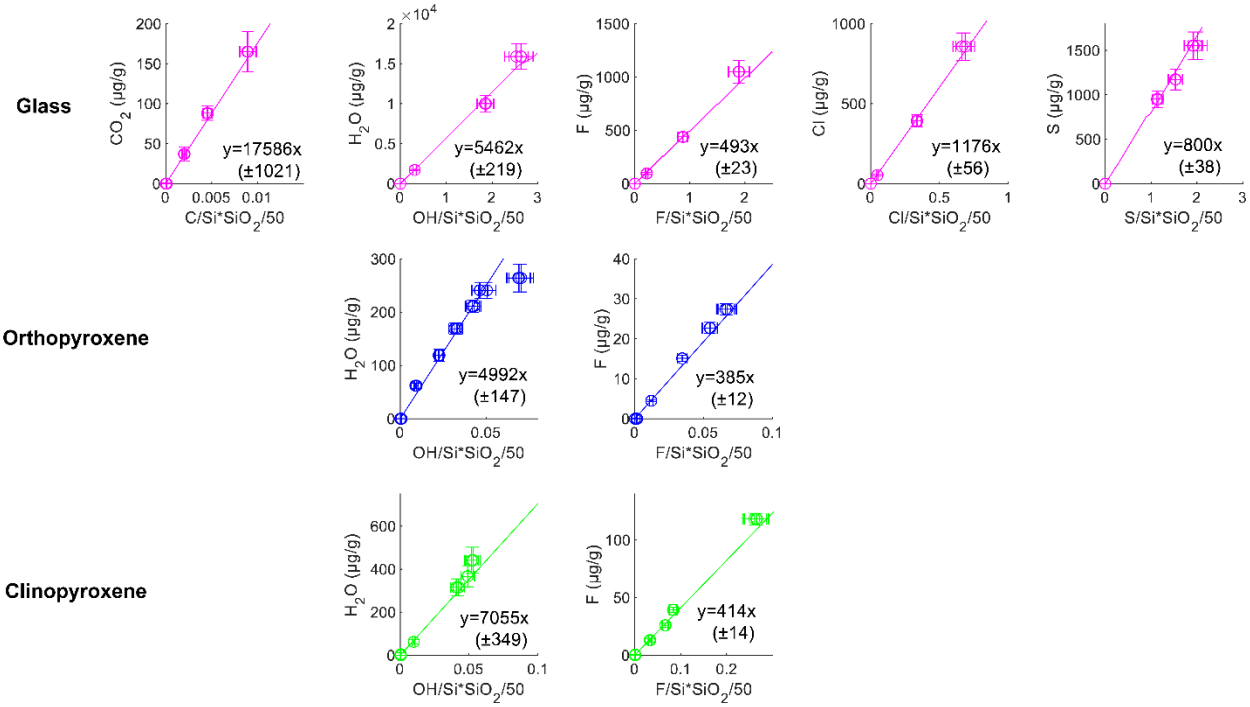

Fig. S2) Calibration curves for CO_2, H_2O, F, Cl, and S for glass, orthopyroxene, and clinopyroxene in the 02/22 analytical session. Uncertainties on slopes were determined using a York regression (Wiens, 2021; York et al., 2004).

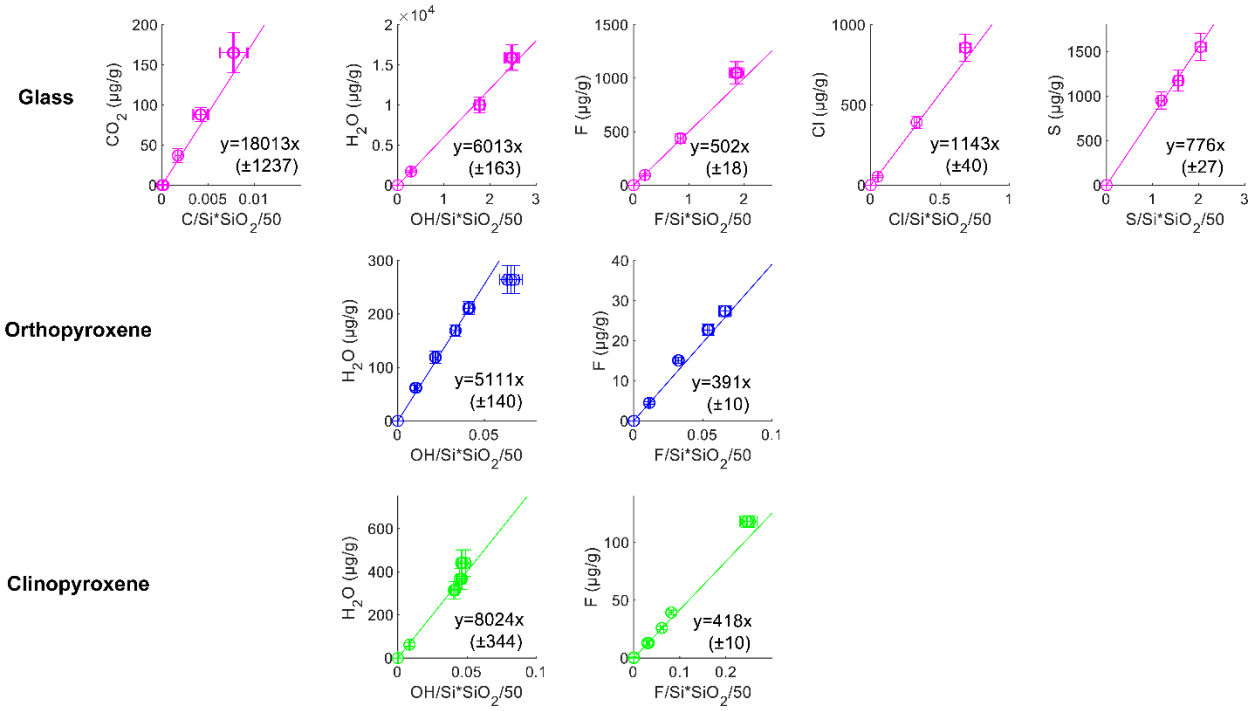

243

244 ***Fig. S3)*** Calibration curves for CO_2, H_2O, F, Cl, and S for glass, orthopyroxene, and

245 clinopyroxene in the 08/22 analytical session. Uncertainties (indicated in parentheses) on slopes

246 were determined using a York regression (Wiens, 2021; York et al., 2004).

247

248

249

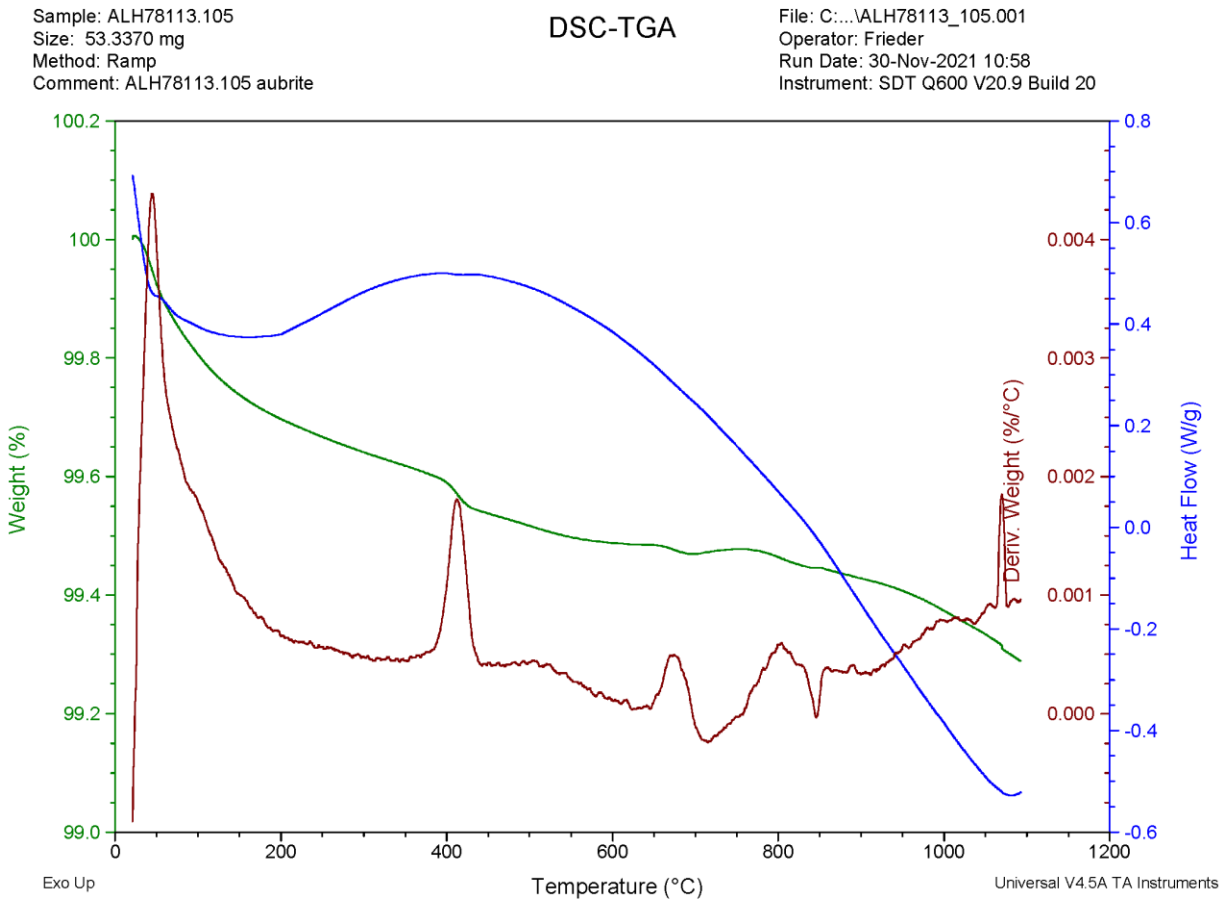

Fig. S4) Mass thermogram for sample ALH 78113. The green line represents mass loss in weight %. The red line represents the first derivative of the mass loss curve. The blue line represents the heat flow throughout the mass loss analysis.

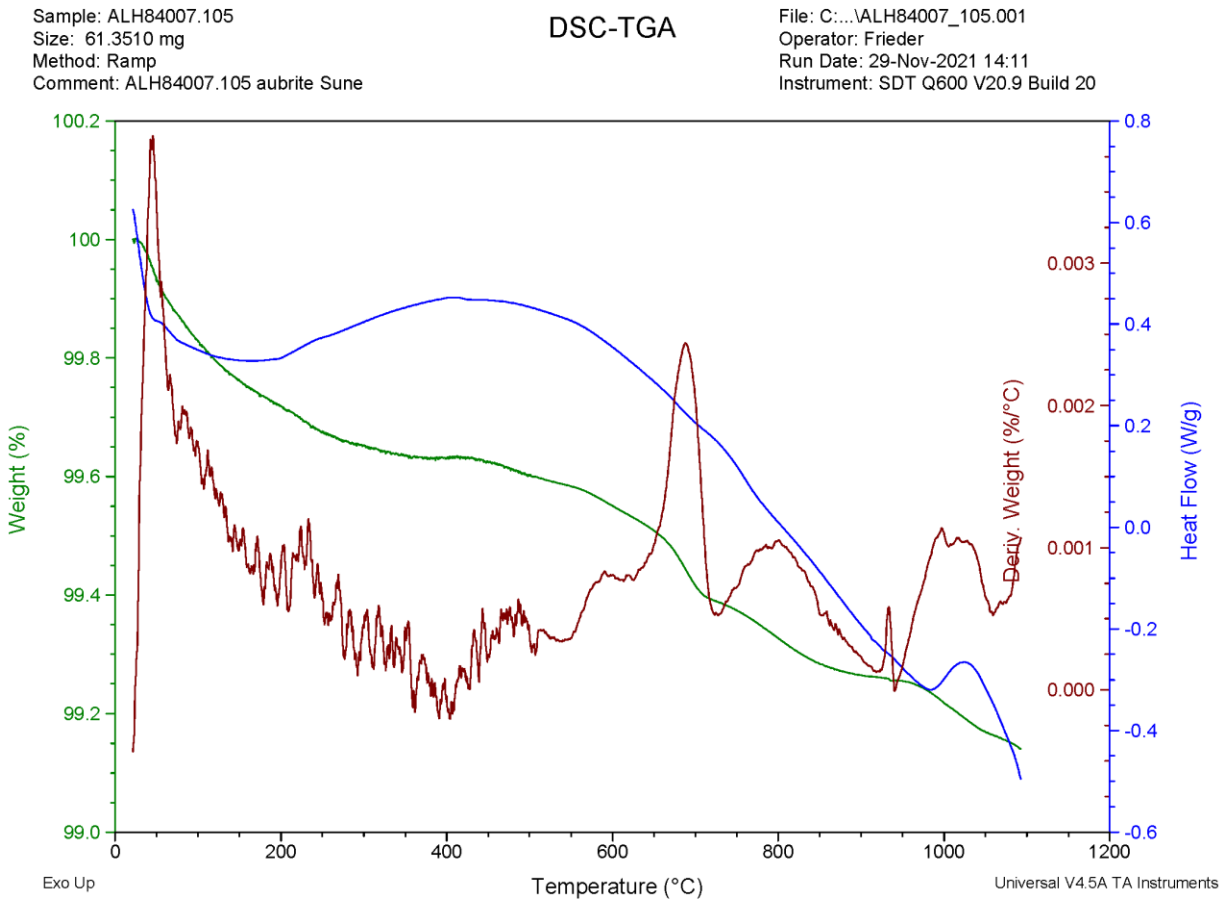

256

257 ***Fig. S5)*** Mass thermogram for sample ALH 84007. The green line represents mass loss in

258 weight %. The red line represents the first derivative of the mass loss curve. The blue line

259 represents the heat flow throughout the mass loss analysis.

260

261

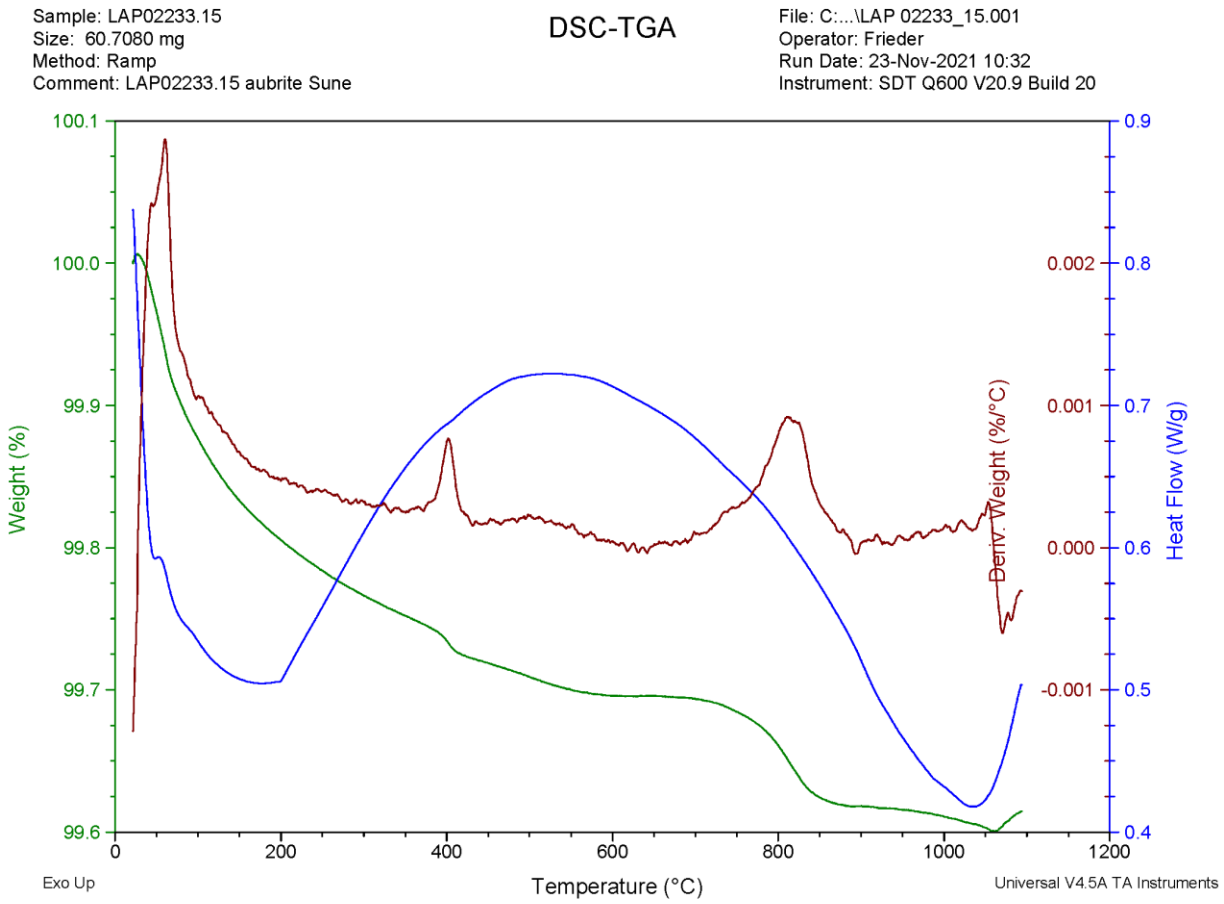

262

263 ***Fig. S6)*** Mass thermogram for sample LAP 02233. The green line represents mass loss in weight

264 %. The red line represents the first derivative of the mass loss curve. The blue line represents the

265 heat flow throughout the mass loss analysis.

266

267

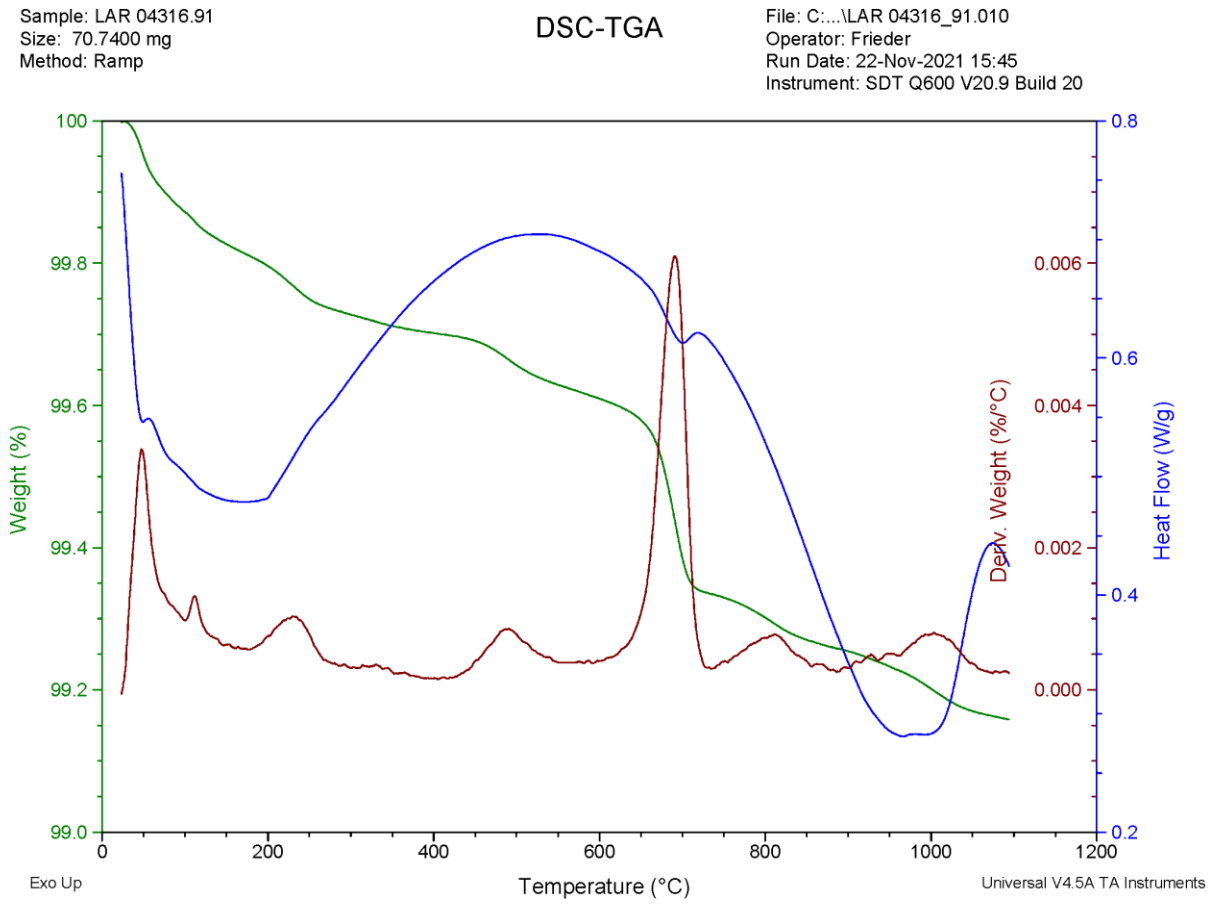

268

269 ***Fig. S7)*** Mass thermogram for sample LAR 04316. The green line represents mass loss in weight

270 %. The red line represents the first derivative of the mass loss curve. The blue line represents the

271 heat flow throughout the mass loss analysis.

272

273

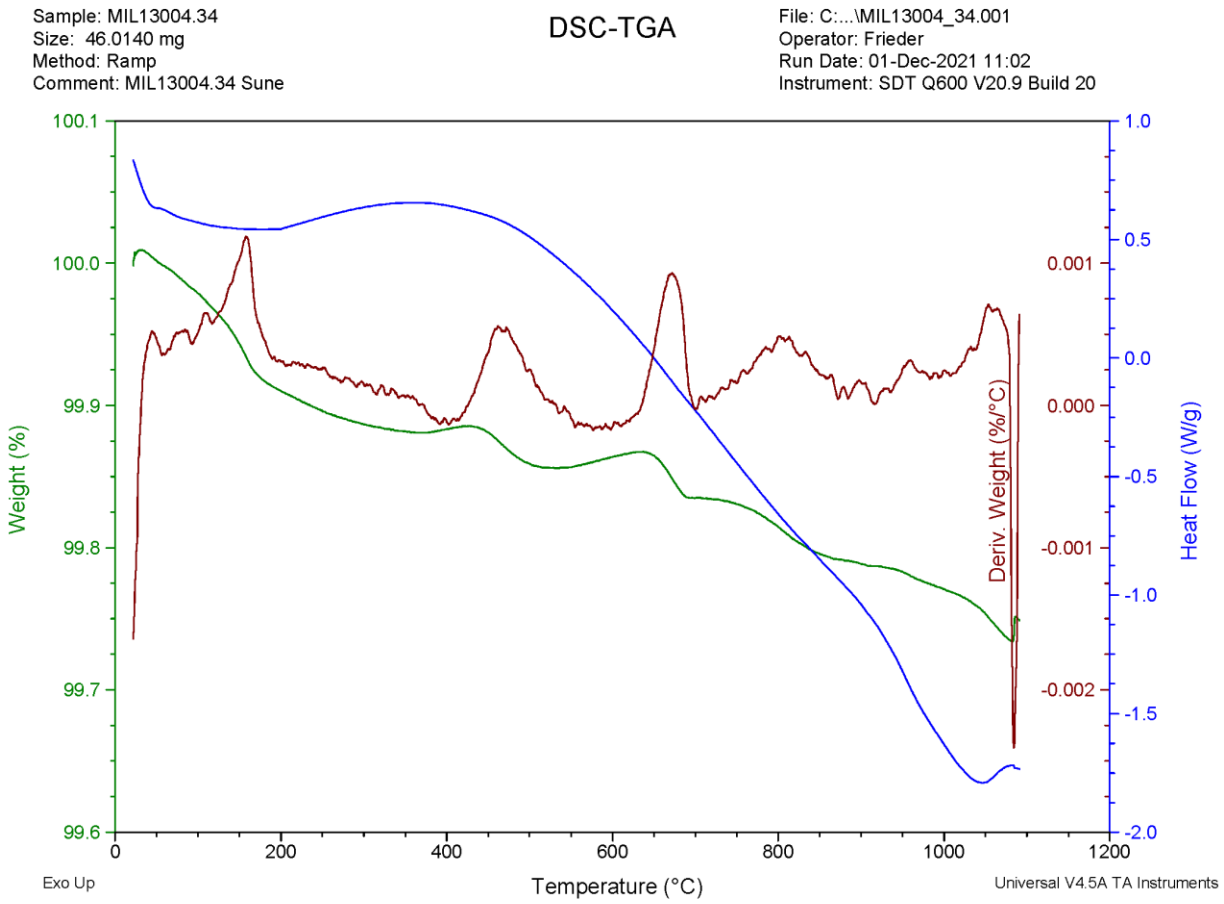

274

275 ***Fig. S8)*** Mass thermogram for sample MIL 13004. The green line represents mass loss in weight

276 %. The red line represents the first derivative of the mass loss curve. The blue line represents the

277 heat flow throughout the mass loss analysis.

278

279

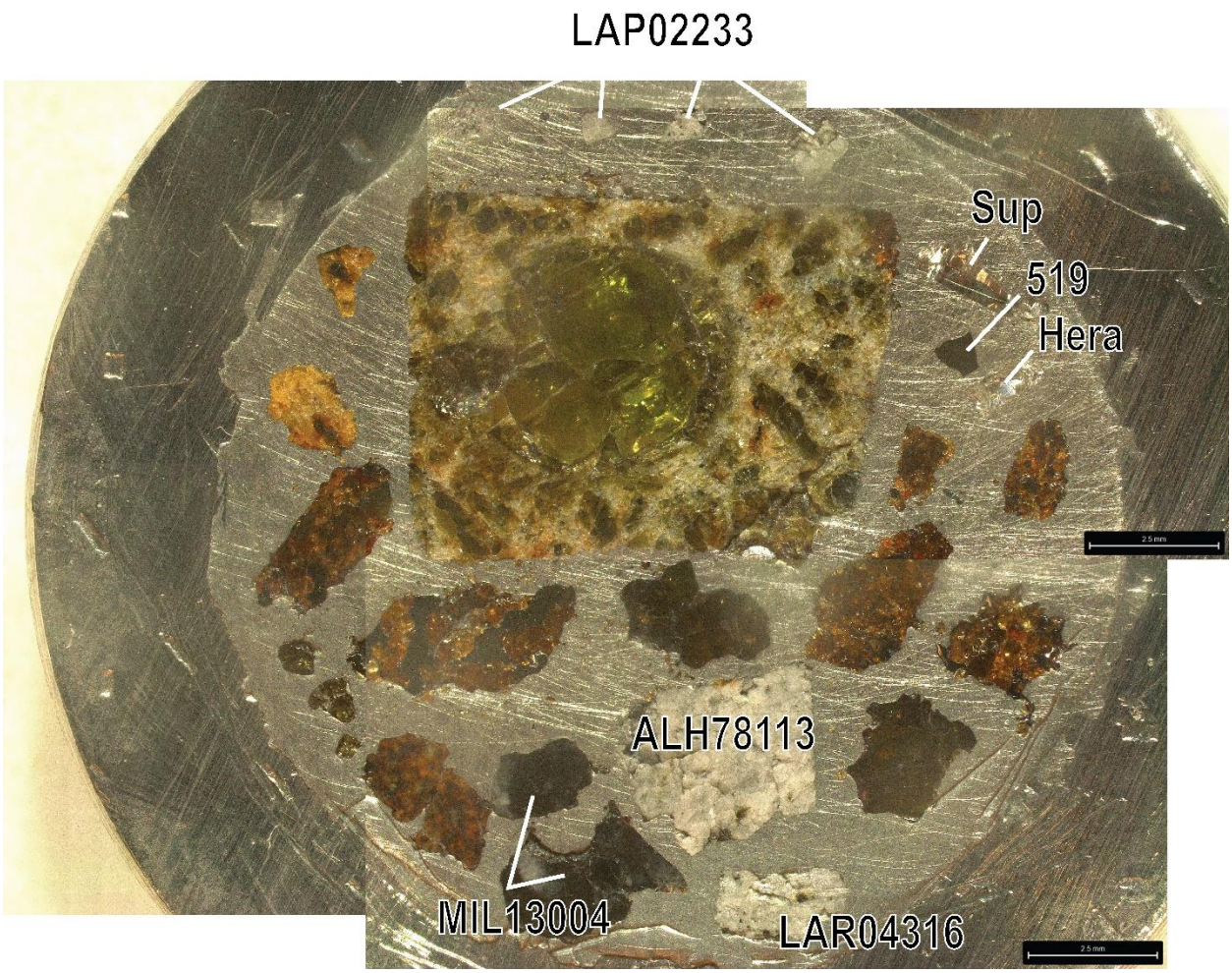

Fig. S9) Reflected light mosaic of 1 inch indium mount containing aubrite samples analyzed as part of this study. Unlabelled samples were not analyzed as part of this study. Scale bars are 2.5 mm.

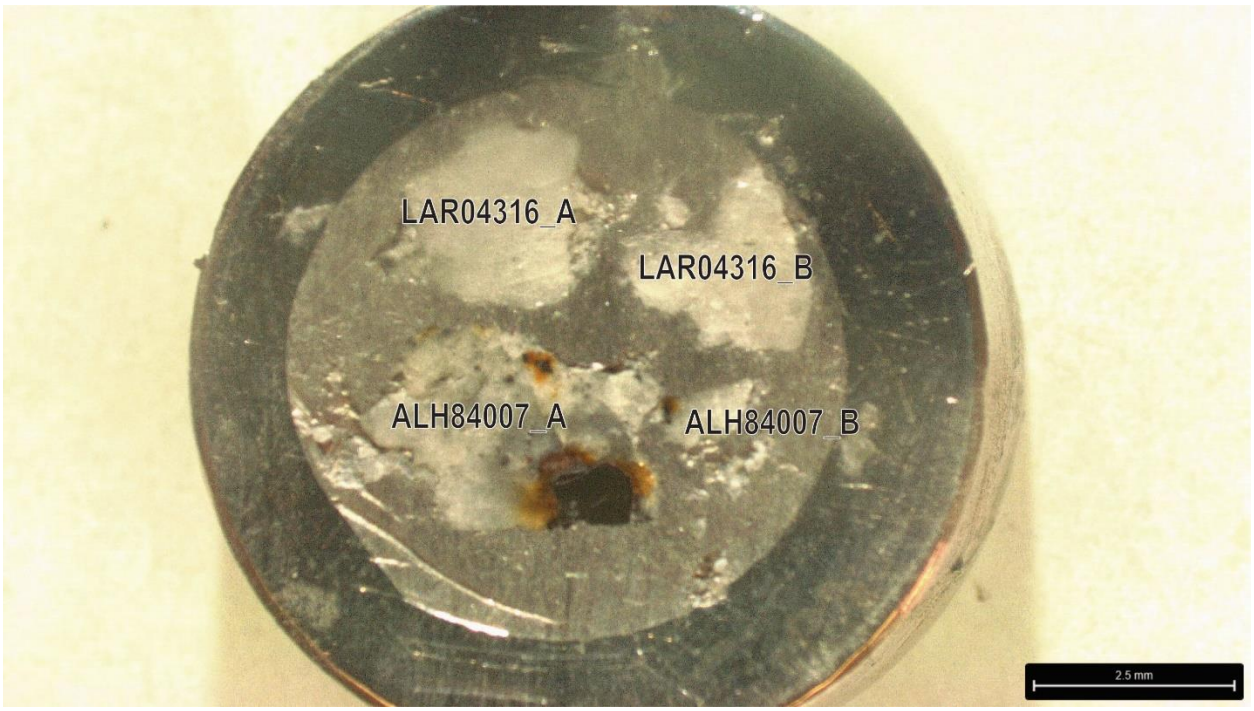

Fig. S10) Reflected light image of 10 mm indium mount holding additional chips of LAR 04316 and ALH 84007. Subsamples are denoted with "_A" and "_B". The scale bar is 2.5 mm.

Fig. S11) Reflected light image of 1 inch indium mount holding Norton County and Shallowater. The three small holes held the secondary standards Suprasil 3002, Herasil, and ALV-519-4-1 glass. The large hole held a sample that was not used in this study.

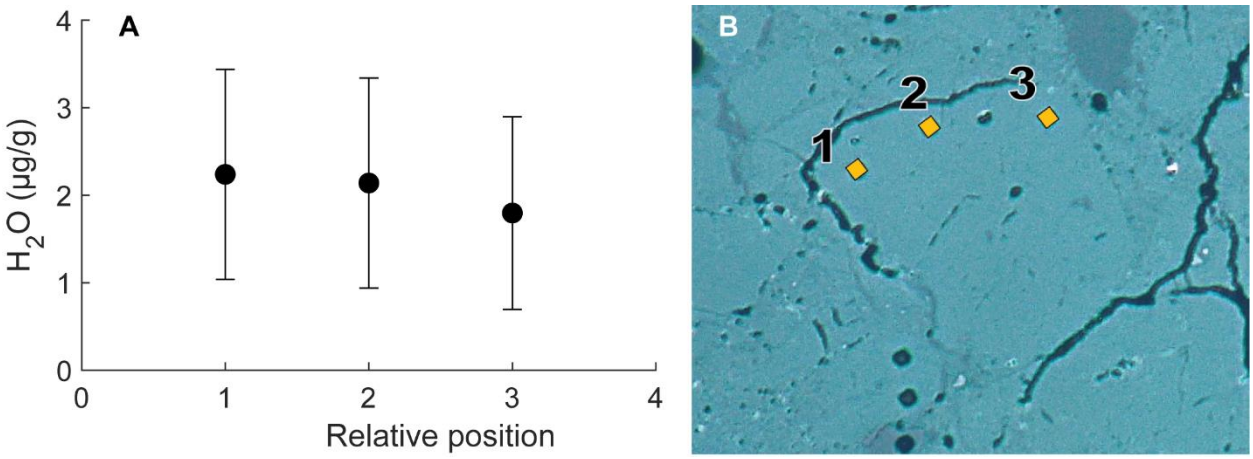

296

297 **Fig. S12)** NanoSIMS transects analyzed for H_2O from grain MIL 13004L-4. A) H_2O
298 concentrations plotted against the relative position of SIMS pits as shown in B). Plotted
299 uncertainties are the propagated uncertainty (Table S3). B) Reflected light image of MIL
300 13004L-4 showing SIMS pits from A) highlighted in orange and labelled. Note, SIMS pits are
301 15×15 µm. The image has a blue tint due to the light used on the microscope and polarizers.
302 Unmarked SIMS pits are associated with other grains or were removed by the data filtering
303 protocol (Section 3.3).

304

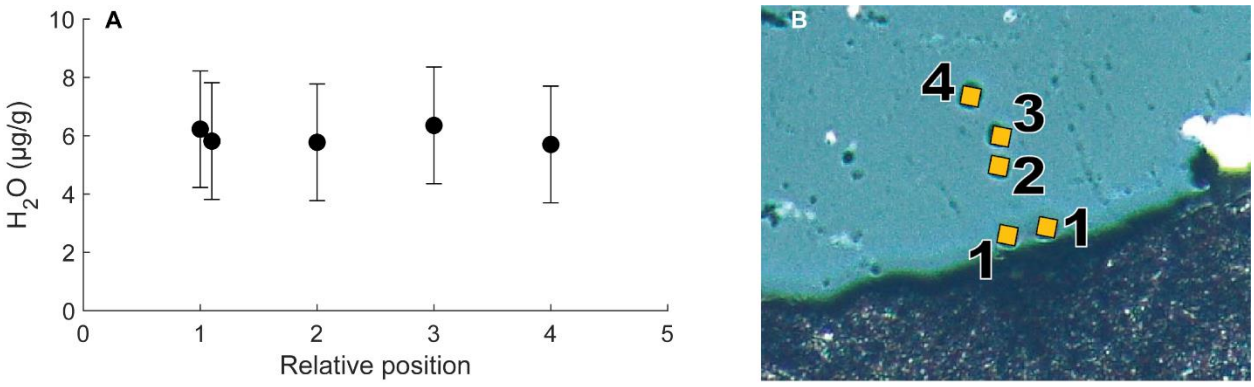

Fig. S13) NanoSIMS transects analyzed for H_2O from grain MIL 13004U-1. A) H_2O concentrations plotted against the relative position of SIMS pits as shown in B). Overlapping points were measured at the same approximate distance from the edge of the grain and represent "duplicate" analyses. Plotted uncertainties are the propagated uncertainty (Table S3). B) Reflected light image of MIL 13004U-1 showing SIMS pits from A) highlighted in orange and labelled. Note, SIMS pits are 15×15 µm. The image has a blue tint due to the light used on the microscope and polarizers.

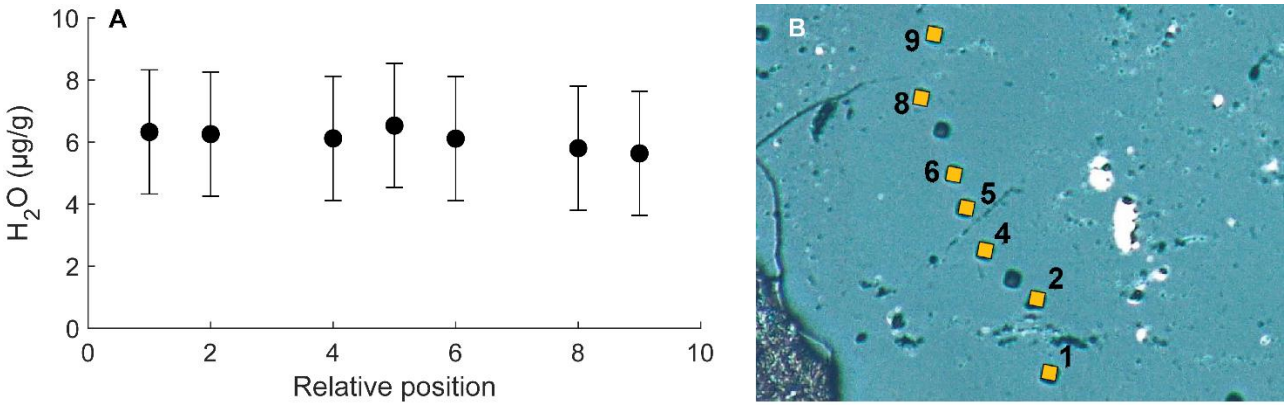

315

316 **Fig. S14)** NanoSIMS transects analyzed for H_2O from grain MIL 13004U-2. A) H_2O

317 concentrations plotted against the relative position of SIMS pits as shown in B). Plotted

318 uncertainties are the propagated uncertainty (Table S3). B) Reflected light image of MIL

319 13004U-2showing SIMS pits from A) highlighted in orange and labelled. Note, SIMS pits are

320 15×15 µm. The image has a blue tint due to the light used on the microscope and polarizers.

321 Unmarked SIMS pits are associated with other grains or were removed by the data filtering

322 protocol (Section 3.3).

323

324

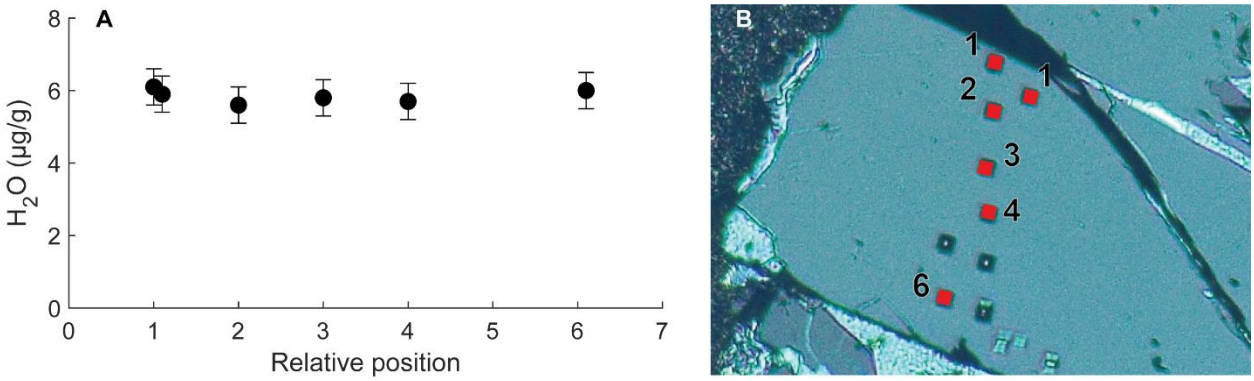

325

326 **Fig. S15)** NanoSIMS transects analyzed for H_2O from grain Shallowater-pyx1. A) H_2O
327 concentrations plotted against the relative position of SIMS pits as shown in B). Overlapping
328 points were measured at the same approximate distance from the edge of the grain and represent
329 "duplicate" analyses. Plotted uncertainties are the propagated uncertainty (Table S7). B)
330 Reflected light image of Shallowater-pyx1 showing SIMS pits from A) highlighted in red and
331 labelled. Note, SIMS pits are 15×15 µm. The image has a blue tint due to the light used on the
332 microscope and polarizers. Unmarked SIMS pits are associated with other grains or were
333 removed by the data filtering protocol (Section 3.3).

334

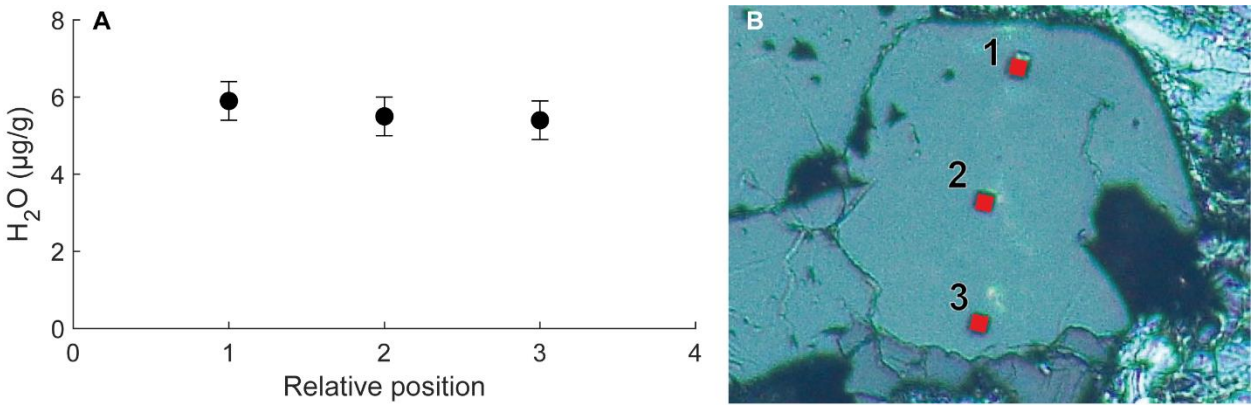

335

336 **Fig. S16)** NanoSIMS transects analyzed for H_2O from grain Shallowater-pyx4. A) H_2O
337 concentrations plotted against the relative position of SIMS pits as shown in B). Overlapping
338 points were measured at the same approximate distance from the edge of the grain and represent
339 "duplicate" analyses. Plotted uncertainties are the propagated uncertainty (Table S7). B)
340 Reflected light image of Shallowater-pyx4 showing SIMS pits from A) highlighted in red and
341 labelled. Note, SIMS pits are 15×15 µm. The image has a blue tint due to the light used on the
342 microscope and polarizers.

343